

Commensurate magnetic structures of RMn_2O_5 ($R=Y, Ho, Bi$) determined by Single-crystal Neutron Diffraction

C. Vecchini,^{1,2} L. C. Chapon,¹ P. J. Brown,³ T. Chatterji,³ S. Park,⁴ S-W. Cheong,⁴ and P. G. Radaelli¹

¹*ISIS Facility, Rutherford Appleton Laboratory, Chilton, Didcot, Oxfordshire, OX11 0QX, United Kingdom.*

²*IESL - FORTH, P.O. Box 1527, Vassilika, Vouton, 711 10 Heraklion, Crete, Greece.*

³*Institut Laue-Langevin, 6, rue Jules Horowitz, BP 156 - 38042 Grenoble Cedex 9 - France.*

⁴*Rutgers Center for Emergent Materials and Department of Physics & Astronomy, Rutgers University, Piscataway, New Jersey 08854, USA.*

(Dated: October 25, 2018)

Abstract

Precise magnetic structures of RMn_2O_5 , with $R = Y, Ho, Bi$ in the commensurate/ferroelectric regime, have been determined by single-crystal neutron diffraction. For each system, the integrated intensities of a large number of independent magnetic Bragg reflections have been measured, allowing unconstrained least-squares refinement of the structures. The analysis confirms the previously reported magnetic configuration in the ab-plane, in particular the existence of zig-zag antiferromagnetic chains. For the Y and Ho compounds additional weak magnetic components parallel to the c-axis were detected which are modulated in phase quadrature with the a-b components. This component is extremely small in the $BiMn_2O_5$ sample, therefore supporting symmetric exchange as the principal mechanism inducing ferroelectricity. For $HoMn_2O_5$, a magnetic ordering of the Ho moments was observed, which is consistent with a super-exchange interaction through the oxygens. For all three compounds, the point symmetry in the magnetically ordered state is m2m, allowing the polar b -axis found experimentally.

PACS numbers: 25.40.Dn, 75.25.+z, 77.80.-e

I. INTRODUCTION

Materials in which there is strong interplay between ferroelectric and magnetic ordering are attracting current interest due to the possibility of controlling the electric polarization by application of a magnetic field or conversely the magnetisation with an electric field. In the last few years, studies have been focussed on systems, such as TbMnO_3 [1, 2] and RMn_2O_5 [3], for which the ferroelectric transition coincides with the transition to a complex antiferromagnetic ordered phase at low-temperature. These systems are classified as *improper* ferroelectrics, since the primary order parameter is the magnetization, and their electrical polarization is at least an order of magnitude lower than in proper ferroelectrics[4]. Nonetheless, the coupling between the magnetization and the electrical polarization is strong, providing an exciting playground in which to study the microscopic mechanisms that govern the magneto-electric interaction. Moreover, the aforementioned systems commonly present a high degree of magnetic frustration, which seems closely linked to the appearance of ferroelectricity[5].

The nature of the low-temperature state in these materials has been investigated by a variety of experimental techniques sensitive to small ionic displacements in a crystal (Raman, IR spectroscopy)[6, 7] and scattering techniques sensitive to the magnetic order (Neutron, resonant X-ray scattering)[8, 9, 10, 11, 12]. An increasing number of theoretical models have also appeared over the last two years that discuss the origin of the magneto-electric coupling[3, 13, 14, 15, 16]. Two microscopic mechanisms have been put forward: on one hand the antisymmetric *inverse* Dzyaloshinskii-Moriya (DM) interaction, requiring a non-collinear magnetic arrangement and on the other hand exchange-striction due to symmetric exchange. In the DM model, the polarization direction \mathbf{P} (atomic displacement direction) is given by the expression:

$$P \propto e_{12} \times (S_1 \times S_2) \tag{1}$$

where S_1 and S_2 are neighboring spins and e_{12} is the propagation direction. The proportionality constant is related to the strength of the spin-orbit coupling. It seems that this mechanism explains the origin of ferroelectricity in many systems recently investigated such as TbMnO_3 [3, 14, 15]. Exchange-striction, which is intrinsically stronger than DM, does not require non-collinearity, and has been proposed to explain the appearance of ferroelectricity in RMn_2O_5 [16] and in the 'E' -phase of HoMnO_3 [17]. Recent work by Infra-Red absorption

confirmed that both mechanisms described above are relevant, as suggested by different polarization selection rules for the electromagnons in $RMnO_3$ and RMn_2O_5 [7]. It is important to note, that due to the extremely small shifts of atoms in the ferroelectric state with respect to their positions in the centro-symmetric paraelectric phase, these displacement patterns have not yet been properly determined. The mechanism which drives the ferroelectric transition can therefore often be more easily inferred from analysis of the magnetic configuration derived from neutron diffraction experiments.

There has been continuing interest in the complex magnetic structures of RMn_2O_5 with $R =$ Rare earth (space group Pbam) since the 1960s [18, 19, 20]. These insulators order antiferromagnetically at low temperature ($T_N \approx 40$ K) with a propagation vector $(k_x, 0, k_z)$ and on further cooling undergo a series of magnetic transitions to both commensurate and incommensurate magnetic phases. These materials become ferroelectric at a temperature slightly below the Néel transition at T_N with values of electric polarization, ranging from 20 to 100 nC.cm⁻² depending on the R ion, being largest in the commensurate phase. The component of the magnetic propagation vector along c (k_z) depends on the size of the R cation, which suggests that the magnetic exchange along the c -direction is extremely sensitive to the interlayer coupling[9, 21]. Bi with $r_I=131$ pm has the largest ionic radius of the series and in $BiMn_2O_5$ $k_z=1/2$ whereas $k_z=1/4$ for YMn_2O_5 , $HoMn_2O_5$ and $TbMn_2O_5$ with $r_I=116,116,118$ pm respectively[32]. On the other hand, the onset and strength of ferroelectricity does not seem to be dependent on r_I .

The magnetic structures of this class of materials have mostly been derived from neutron diffraction on polycrystalline samples. Recently however, Noda and co-workers have reported results obtained by single-crystal neutron diffraction for the commensurate magnetic phase of YMn_2O_5 [8]. Their analysis suggested the presence of a small c -axis component of magnetic moment on the Mn sites, which had not been detected in previous powder measurements[16]. This additional component is in phase quadrature with the major a-b component and introduces a cycloidal modulation of the magnetic moments which could, in principle, induce ferroelectric order through the DM interaction.

In the light of this recent work, we have undertaken determination of the commensurate magnetic structures of three compounds $BiMn_2O_5$, YMn_2O_5 and $HoMn_2O_5$ using single-crystal neutron diffraction. Variation of the cations allows a comparative study in which their influence on various characteristics of the magnetic structures can be distinguished.

The aim of the study is twofold: first to search systematically for the presence of the c -axis modulation in several members of the series so as to gauge its importance in promoting ferroelectricity. Determination of the magnitude of this component for all three compounds is especially important because the magnetic propagation vector in BiMn_2O_5 ($k_z=\frac{1}{2}$) differs from that in HoMn_2O_5 and YMn_2O_5 ($k_z=\frac{1}{4}$). Secondly, by studying HoMn_2O_5 , we can investigate the influence of a magnetic R ion on the arrangement of the Mn moments and determine the magnetic ordering of the Ho sublattice itself. Comparison with YMn_2O_5 , which has the same propagation vector but a non-magnetic R site is of particular interest, since the values of the electric polarization in the commensurate regime of the two systems are significantly different.

II. EXPERIMENT

Single crystals of RMn_2O_5 ($R=\text{Bi}, \text{Y}, \text{Ho}$) were grown using $\text{B}_2\text{O}_3/\text{PbO}/\text{PbF}_2$ flux in a Pt crucible. The flux was held at $1,280^\circ\text{C}$ for 15 hours and slowly cooled down to 950°C at a rate of 1°C per hour. Crystals grew in the form of cubes. The samples used for the present work were respectively of sizes: $\sim 4\text{x}4\text{x}4 \text{ mm}^3$ for YMn_2O_5 , $2\text{x}2\text{x}2 \text{ mm}^3$ for HoMn_2O_5 and $1\text{x}1\text{x}3 \text{ mm}^3$ for BiMn_2O_5 , where the three dimensions refer to the $[110]$, $[\bar{1}10]$ and $[001]$ directions. For the HoMn_2O_5 crystal, additional faces (100) and (010) were also visible. Single crystal diffraction measurements were performed on the four-circle diffractometer D10 at the ILL (Grenoble, France). Samples were checked for quality and pre-aligned with the (001) direction oriented along the vertical axis using the OrientExpress facility (ILL). Samples were mounted on standard aluminum pins in a He exchange gas cryostat. Data were collected with an incident neutron wavelength of $\lambda = 2.36 \text{ \AA}$ using an 80 mm^2 2D micro-strip detector. Ω scans around each Bragg reflection were performed, with variable counting time depending on the intensity. Peak integration was performed using the program *Racer* (ILL), in two steps. First, a library was built by fitting ellipsoidal shapes to a set of strong reflections ($I>3\sigma$), these shapes were used in a second pass to integrate all reflections. Data were collected for all three samples in the ordered magnetic commensurate phases. An additional dataset was collected for the YMn_2O_5 sample in the low-temperature incommensurate phase, but the results will be reported elsewhere. The data sets for YMn_2O_5 were collected at $T = 25 \text{ K}$ (nuclear and magnetic scattering), those

for BiMn_2O_5 at $T = 10$ K (nuclear and magnetic scattering) and for HoMn_2O_5 at $T = 50$ K (nuclear scattering) and $T = 25$ K (magnetic scattering). For each data-set, the list of integrated intensities obtained were corrected for Lorentz-factors and normalized to an arbitrary monitor count. Determination of both the nuclear and magnetic structures were carried out using the FullProf program suite[22]. For each sample the following procedure was applied: the published crystallographic models, space group $Pbam$ were used to refine the nuclear data-sets. Because a limited Q-range is accessible on D10, the crystallographic parameters were fixed, with the exception of a global thermal parameter to account for different temperatures. In addition, a global scale factor was refined together with six parameters for extinction correction, following the formulation of Becker-Coppens for anisotropic extinction (extinction model number 4 in FullProf). This correction is particularly important for YMn_2O_5 because of the large size of the crystal. The scale factors obtained by refining the nuclear structure were used and fixed for refinement of the magnetic structures.

III. RESULTS

A. Crystal structure and formalism

The crystal structure and topology of the magnetic interactions have been described in detail in [16, 23]. The different atomic positions for Mn^{3+} , Mn^{4+} (and Ho^{3+}) have been numbered according to reference [23]. To facilitate the identification of all magnetic sites in the figures, additional labels have been included: a for Mn^{3+} , b for Mn^{4+} (c for Ho^{3+}). The crystal structure of RMn_2O_5 (isostructural throughout the series) is displayed in Fig. 2 and the correspondence between labels and atomic positions can be found in table II. Mn^{3+} (a) is five-coordinated by oxygen ions, in square-pyramid geometry, while Mn^{4+} (b) is six-coordinated in distorted octahedral geometry. There are four symmetry equivalent Mn^{3+} sites and four Mn^{4+} sites per unit-cell. The pyramids centered at a2 and a3 (also a1 and a4) share an edge of their basal plane. All Mn^{3+} are located on a mirror plane at $z=0.5$. The octahedra coordinating the Mn^{4+} sites b1 and b2 (also b3 and b4) share edges to form chains running along the c -direction. The b1(b3) atoms with $z\sim 0.25$ and b2(b4)

with $(1-z) \sim 0.75$ lie below and above the Mn^{3+} layer. It should be noted that the sites b_1 and b_2 also b_3 and b_4 are related by a center of symmetry. The Mn^{4+} octahedra share corners with Mn^{3+}O_5 pyramids to form layers in the ab -plane. The R ions (labeled c for HoMn_2O_5) occupy the $(x,y,0)$ site, of multiplicity four, and are all positioned in the $z=0$ layer separating two $\text{Mn}^{3+}/\text{Mn}^{4+}$ layers.

The magnetic structures have been analyzed using the propagation-vector formalism, in which magnetic moments for all sites described above are expanded in Fourier series. We briefly describe the conventions used in the next paragraph. For a magnetic structure with a single propagation vector \vec{k} , which is the relevant case in this study, a magnetic moment of atom type j in the crystallographic unit-cell l (\vec{m}_{lj}) is written:

$$\vec{m}_{lj} = \sum_k \vec{S}_{kj} \cdot e^{-2\pi \cdot i \cdot (\vec{k} \cdot \vec{R}_l + \phi_j)} \quad (2)$$

where the sum runs over \vec{k} and $-\vec{k}$ if these vectors are not related by a reciprocal lattice vector (case of YMn_2O_5 and HoMn_2O_5) or uniquely \vec{k} otherwise (case of BiMn_2O_5). \vec{R}_l is a pure lattice translation and ϕ_j is a phase factor. The magnetic structure is fully determined by giving a set of Fourier coefficients and phases (\vec{S}_{kj}, ϕ_j) for each j , i.e seven components per site in the most general case since the Fourier coefficients are complex quantities. We note that because \vec{m}_{lj} is a real quantity, the constraint $\vec{S}_{-kj} = \vec{S}_{kj}^*$ (where $*$ denotes the complex conjugate) is required. It is important to mention that ϕ_j are relative phases and are equal for sites belonging to the same orbit, i.e. sites that can be transformed into each other by an operation of the magnetic little group. It is different than a global phase, that can't be determined by diffraction, which rephase the entire magnetic structure, i.e. apply simultaneously to all magnetic sites. Additional constraints exist between (\vec{S}_{kj}, ϕ_j) of symmetry-related sites. These constraints are determined by representation analysis and will be briefly described in the following sections, based on previously published work[24].

B. YMn_2O_5

1. *Magnetic structure*

The propagation vector for the Y-compound in the commensurate phase (CM) is $\vec{k}=(1/2, 0, 1/4)$. Symmetry analysis [24] indicates that the Mn^{4+} sites is split into two orbits because the m_z mirror-plane operation does not belong to the little group. The first and second orbits contain respectively the b1/b3 sites and b2/b4 sites. The ϕ_j phases for each orbit can therefore be non-equal and treated as free parameters during the refinement. On the other hand, the phases of the Mn^{3+} sites, belonging to a single orbit, must be equal. We arbitrarily chose to fix the phase of the Mn^{3+} sites at 0.125 (one phase must be fixed since structure factors do not depend on a global phase), for comparison with results reported earlier from powder data [16] describing a configuration with equal moments. In this case, representation analysis does not impose any constraints on the magnitude and direction of the Fourier coefficients for both Mn^{3+} and Mn^{4+} sites[24]. For each site, six independent Fourier coefficients are in principle refinable. The unconstrained model has therefore fifty parameters and describe the most general magnetic structure. For typical magnetic structures described by either spin-density waves (SDW) or simple cycloidal modulations, some of these parameters will be fully correlated. Refining an unconstrained model against the 355 independent magnetic reflections fails due to the large number of parameters and the presence of strong correlations. In order to find possible models, a global optimization algorithm, using the simulated annealing procedure described in [25], was employed. Systematically, the Fourier coefficients for all magnetic sites were found to be principally along the a -axis, whether real or imaginary. In addition, a weaker b -axis component was found with the same character (real or imaginary) as the a -component. These two components define a vector, say \mathbf{v}_1 in the ab -plane. A small c -axis component in phase quadrature with the a and b -components was also identified. The structure therefore has a small helicoidal modulation, with rotation axis given by the cross product of \mathbf{v}_1 with a vector along z . A model with this configuration, i.e one in which the Fourier coefficients for all magnetic sites are real in the ab -plane and imaginary along c , has been constructed, it has 26 refinable parameters. The lower number of free parameters allowed a direct least-square refinement to be made which converged after a few cycles. The structure factors calculated with this model are shown, plotted against

those observed, in Fig. 1. The model was found to reproduce the observed data very well with a Magnetic R(F) factor[33] of 4.57% (Fig. 1). For this particular sample, the large value of $\chi^2=163$ is explained by high statistics of the data obtained on a large sample with long counting time. The refined values of the Fourier coefficients are displayed in Table II and the magnetic structure projected along two different crystallographic directions in Fig. 3 and Fig. 4. The magnetic arrangement in the ab -plane (Fig. 3) is equivalent to that derived in our previous work from powder data[16]. The moment directions are within $\sim 10^\circ$ of the a -axis for Mn^{3+} and $\sim 14^\circ$ for Mn^{4+} , defining zig-zag antiferromagnetic (AFM) chains running along a . One of these chains links b1, b2, a2 and a3, the other b3, b4, a4 and a1. In addition, there is a significant c -component on all magnetic sites as suggested by Noda et al.[8], which was not found in our earlier analysis of powder data. The c -components have almost the same magnitude as the b -components on both Mn sites. Their imaginary character means that the modulation is in quadrature with the real *in-plane* components. This can be seen in Fig. 4; for example for the a2 site the in-plane components of the magnetic moment follow a (- + + -) sequence across four unit-cells along c whilst the c -component follows a (- - + +) sequence. This result is also in agreement with the work of Noda et al. The refined values of the phases for sites b1/b3 and b2/b4, respectively 0.095(2) and 0.156(2), are slightly different from the fixed values of 0.125 used for fitting powder data. Consequently, and in addition to the existence of a c - component, the magnetic moments on site b1 and b2 (as well as b3 and b4) are of different magnitudes as shown in Fig 4. We also note that there is a symmetric deviation of these phases with respect to Mn^{3+} phase of 0.125 ($(0.125-\delta)$ for the first orbit and $(0.125+\delta)$ for the second orbit). The identification of a small c -component has direct implications on the nature of the magnetic configuration, previously described as a pure SDW: small cycloidal modulations propagating along the edge-sharing Mn^{4+}O_6 chains are observed in the ac and bc -planes (Fig. 5). In the ac -plane, the moment rotation direction is clockwise for Mn^{4+} chains formed by the b1 and b2 sites (left panel of Fig. 4) and anti-clockwise for chains formed by the b3 and b4 sites (right panel of Fig. 4). In the bc -plane, the weak cycloidal modulation, highlighted in Fig. 5, rotates in the same direction along b1/b2 chains and b3/b4 chains. The Mn^{3+} moments are also slightly tilted along the c -direction, remaining almost collinear to adjacent Mn^{4+} magnetic moments in a given AFM chain. Therefore, the presence of antiferromagnetic chains running along the a -axis, identified earlier as an important characteristic of these systems, remain valid despite

the small c -component.

2. Domains

The arm of the star of k is made only of the two vectors $\vec{k}=(\frac{1}{2},0,\frac{1}{4})$ and $-\vec{k}$ since the vectors $(-\frac{1}{2},0,\frac{1}{4})$ and $(\frac{1}{2},0,-\frac{1}{4})$ are related to k and $-k$ by a reciprocal lattice vector. Therefore, a single k -domain contributes to the scattering. On the other hand, one must take into account the "orientation" domains, i.e. domains that are obtained by applying symmetry operations of the paramagnetic group that are not valid operations (lost) of the magnetic structure. Four symmetry operations of the paramagnetic group (combined or not with complex conjugation) leaves the magnetic structure unchanged, as shown in Table I. We refer to this domain as domain one (D1). The other four symmetry operations all transform the magnetic structure described in the previous section into an inequivalent one (domain 2, D2, shown in Fig. 6). No other domains exist, and D1 and D2 are simply related by inversion symmetry. Inversion symmetry operates differently on different magnetic sites: for b_3, b_4, a_1 and a_4 , belonging to one of the zig-zag AFM chain, the application of inversion symmetry leaves the a and b moment components unchanged while it changes the sign of the c -component. In contrast for sites b_1, b_2, a_2 and a_3 (the other AFM chain), inversion symmetry reverses the sign of the a and b components while preserving the c component. Since D1 and D2 are related by inversion symmetry, the diffracted intensities arising from both domains are identical for a non-polarized diffraction experiment and refining the data assuming any domain leads to the same result. We note that the two domains are also related by a simple rotation by 180° along the z -axis or the x -axis.

From the list of symmetry operations (Table. I) that leave the magnetic structure invariant (modulo complex conjugation operation), one derives the point group $m2m$ in the magnetically ordered phase, in agreement with that obtained earlier from co-representation analysis[24]. This point group is compatible with ferroelectricity along the b -axis, irrespective of the microscopic magneto-electric mechanism.

C. HoMn₂O₅

HoMn₂O₅ orders AFM at T = 44 K first with an incommensurate propagation vector $\vec{k}=(0.48, 0, 0.245)$, followed by a lock-in at T = 38 K to a commensurate $\vec{k}=(\frac{1}{2}, 0, \frac{1}{4})$. The magnetic structure has been determined in the commensurate phase from 381 independent magnetic reflections, using the same procedure as that described in the case of YMn₂O₅. However in this case, the magnetic ordering of Ho is an additional complexity which increases the number of free parameters. Attempting to refine the data without a magnetic contribution on the Ho sites, leads to poor agreement factors (R(F)=20.2%) as already reported from analyzing powder diffraction patterns[23]. Preliminary measurements with resonant X-ray scattering at the L_{III} edge directly confirm the magnetic ordering of Ho. Symmetry analysis indicates that the four equivalent Ho positions belong to the same orbit and therefore only one phase parameter is required. However, there are no constraints between components of the moment of different sites, which were refined independently. The final refinement contained 45 parameters and was found to reproduce the data very well with structure factor R(F)=3.96% and $\chi^2=5.82$. The magnetic structure is similar to the YMn₂O₅ one, with the appearance of almost collinear ...-Mn⁴⁺-Mn³⁺-Mn³⁺-Mn⁴⁺-... AFM zig-zag chains in the *ab*-plane. These chains make an angle of $\sim 14^\circ$ with respect to the *a*-axis. We again found a small *c*-component (Fig. 8) of moment on all Mn magnetic sites, in quadrature with the in-plane components and of magnitude similar to that observed for YMn₂O₅. The refined phase for the Ho sites is shifted by 0.126(2) with respect to the Mn³⁺ sites. The Ho moments at the c3/c4 sites are parallel to the *a*-axis and those at the c1/c2 sites to the *b*-axis (Fig. 7 and Table. III). It is possible that a smaller, $\pi/2$ out of phase component along *c* may exist, but the refined magnitudes are only three times larger than the error bars. Although the magnetic configuration of the Ho sites is identical to that derived earlier by simulated annealing using powder data[23], the orientation of the Ho moments in the *ab*-plane is quite different. The values of the Ho moments, ranging from 1.1 to 1.3 μ_B , are much smaller than the fully saturated value for a J=8 state. This can be partly explained by splitting of the fully degenerate J=8 state by the crystal field, but typical crystal-field energies in oxides will lead to a moment much larger than observed here[26]. Additional reduction can be due thermal excitation, at 25K, of levels above the ground state (Ho³⁺ is a non-Kramer ion characterized by singlet levels). Moreover, dipolar

field calculations show no direct correlation between the local field generated by neighbors magnetic Mn sites and the magnitude and direction of the Ho moments. Therefore we argue that the Ho moment of $\sim 1.1\mu_B$ in HoMn_2O_5 is mainly due to super-exchange interactions via the 2p oxygen orbitals. Exactly half of the Ho layers show ordered magnetic moments in the ab -plane, while the other half show only a small moment along the c -direction (Fig. 8). Accordingly, in the former type of layers, we can clearly show that the directions of the moment are systematically arranged along the resultant of AFM super-exchange interactions with the four nearest-neighbor Mn^{4+} sites (Fig. 7 and Fig. 8). The net moment on each Ho sites is pointing either along the a -axis (sites c3 and c4) or b -axis (sites c1 and c2), resulting from the cancelation of respectively the b - and a -components of neighbor Mn^{4+} moments. Also, the resultant of the super-exchange is larger for sites c3 and c4 (along the a -direction) than for sites c1 and c2 (along b), which should lead to different Ho moments on these sites, as we appear to observe experimentally (Table III). A more precise determination of the respective magnitude of the moments on sites c1/c2 and c3/c4 is currently underway by resonant X-ray scattering. Calculations show that azimuthal scans on magnetic Bragg peaks at the Ho L_{III} edge are extremely sensitive to these parameters (as well as being Ho selective).

The magnetic configuration of the Ho sublattice also breaks inversion symmetry since moments on sites c2 and c3 (respectively c1 and c4) are pointing in different directions. As in the case of YMn_2O_5 , there are only two "orientation" domains to consider, related by inversion symmetry and therefore contributing equally to the diffracted intensities. The symmetry operations and corresponding domains listed in Table I are also valid for HoMn_2O_5 . The magnetic structure of domain 2 including the transformed Ho moments (not shown) is easily derived from domain 1 by applying inversion symmetry. In this case, the magnetic point group is also $m2m$, which supports ferroelectricity along the b -axis.

D. BiMn_2O_5

BiMn_2O_5 is the only member of the series that shows magnetic ordering below $T=39$ K with a propagation vector $\vec{k}=(\frac{1}{2}, 0, \frac{1}{2})$ and no transitions to incommensurate magnetic order. Because of the commensurate propagation vector representation analysis leads to stricter constraints than those applicable to YMn_2O_5 and HoMn_2O_5 , they are described in detail by

Munoz et al.[21]. No phases are required at any of the sites since \vec{k} is half a reciprocal lattice vector. The magnetic representation contains two irreducible representations of dimension 2. Only magnetic modes belonging to the representation Γ_1 fit our single crystal data, in agreement with the results of Munoz et al. The magnetic moments on Mn^{4+} sites are constrained in the following way: sites b1 and b2 have the same a and b components but opposite c components. The same relation holds for sites b3 and b4. However, there are no relationships imposed by symmetry between the two set of sites mentioned above, b1/b2 on one hand and b3/b4 on the other. For the Mn^{3+} sites, the moments are constrained to lie in the ab -plane but can have any magnitude and orientation within it. In the work of Munoz et al., the additional physical constraint of equal moments, not imposed by symmetry, was introduced. Here, the large number of independent magnetic reflections collected (204) allows the simultaneous refinement of all fourteen parameters. The result of the refinement is shown in Fig. 1 and the corresponding magnetic structure is displayed in Fig. 9 and Fig. 10. A R(F) factor of 4.5% has been obtained with a χ^2 value of 18.2. BiMn_2O_5 has a very similar magnetic structure to that described previously for YMn_2O_5 , for instance the antiferromagnetic $\dots\text{Mn}^{4+}\text{-Mn}^{3+}\text{-Mn}^{3+}\text{-Mn}^{4+}\dots$ chains in the ab -plane. This is at variance with the structure proposed by Munoz, in which there is a non-collinear arrangement of Mn^{4+} and Mn^{3+} moments within one AFM chain. The angular deviation of the AFM chains from the a -axis ($\sim 8^\circ$) is less pronounced than in the YMn_2O_5 and HoMn_2O_5 compounds. Also unlike YMn_2O_5 and HoMn_2O_5 , we found almost zero z -components for the Mn^{4+} moments. The magnetic point group is $m2m$ and the magnetic structures of the two possible domains are related by inversion symmetry, as previously described, resulting in flipping the central AFM chain in Fig. 9.

IV. ORIGIN OF FERROELECTRICITY

In this section, we discuss the possible mechanism that will promote a ferroelectric state in the magnetically ordered phase. First of all it is worth noting that irrespective of the microscopic mechanism involved, the point group symmetry $m2m$ derived from the magnetic structures of YMn_2O_5 , HoMn_2O_5 , and BiMn_2O_5 , is consistent with ferroelectric order only along the b -axis. Secondly, it is important to discuss the possible microscopic mechanisms, in the light of the additional weak magnetic components observed along the c -axis for YMn_2O_5

and HoMn_2O_5 and not identified previously by powder diffraction. This small out of plane component introduces a modulation that resembles a cycloid, even though it does not correspond to a homogeneous rotation from site to site, as seen in Fig. 4 for example. However, this modulation could in principle give rise to ferroelectricity based on antisymmetric exchange interaction, a mechanism proposed in several multiferroics, and its strength will be proportional to the spin-orbit coupling, potentially large for octahedral Mn^{4+} . Obviously, the absence of such a modulation in BiMn_2O_5 , multiferroic with a value of the electrical polarization comparable to YMn_2O_5 and HoMn_2O_5 , does not support this picture. Therefore we argue that our model based on symmetric-exchange, and proposed initially in [27], is the principal mechanism driving ferroelectric order. The recent observation of electromagnons[28] active only for certain polarization directions, also supports a model based on symmetric-exchange interaction. This model is relevant since the magnetic configuration in the ab -plane for the three compounds studied here is frustrated, i.e. the magnetic energy is invariant by flipping any AFM chain in the lattice. Such a configuration will induce atomic displacements on some of the ions in the crystal (we speculated that mainly Mn^{3+} ions are involved based on structural anomalies related to this site) that will lower the magnetic energy[6, 16, 29]. This comes at the cost of elastic energy, quadratic with the displacement, but for small displacements the gain in magnetic energy (linear with displacements) overcomes the elastic energy cost. Magneto-striction due to symmetric exchange should be much stronger than the DM interaction, which is a relativistic effect[14, 15, 30]. However, it is possible that this later mechanism contributes to the total electric polarization in the YMn_2O_5 and HoMn_2O_5 compounds but should be of minor importance. In fact, the two mechanisms are likely to be strongly coupled. It is important to note that applying the inversion symmetry operation not only flips one of the AFM chains but also changes the rotation direction of the cycloidal modulation. Therefore the direction of the electric polarization in domain two is opposite to that in domain one, whatever the mechanism considered. The observation of cycloidal structures for many of these compounds is intriguing, and is unlikely to be a coincidence. In general, two mechanisms are known to generate helicoidal-type structures; competition between nearest and next-nearest neighbor interaction and direct DM interaction, resulting from the loss of a center of symmetry relating magnetic ions. It is easy to show that in none of the magnetic structures described here does the cycloidal modulation lower the next-near neighbor magnetic energy, regardless of the sign of the interaction. This

suggests that the observed c -axis modulation may be the effect, rather than the cause, of the loss of the center of symmetry relating Mn^{4+} ions.

V. SUMMARY

The magnetic structures in the ferroelectric/commensurate magnetic regime of three compounds of the family RMn_2O_5 with $R = \text{Y}, \text{Ho},$ and Bi , have been determined by single crystal neutron diffraction. For YMn_2O_5 and HoMn_2O_5 the main features of the magnetic structures are in agreement with previous models derived from powder neutron diffraction characterised, in particular, by collinear antiferromagnetic zig-zag chains in the ab -plane. An additional small component of moment parallel to the c -axis, and modulated in quadrature with the major components has been identified. This component was not detected in earlier experiments. The data also allow a more precise determination of the directions of the Ho magnetic moments. These results indicate the importance of super-exchange interactions in the magnetic ordering of Ho. The magnetic structure of BiMn_2O_5 is very similar to that of the Y and Ho analogs, but with the magnetic moments more closely confined to the ab -plane. It also contains zig-zag AFM chains, in disagreement with what was previously reported[21]. This comparative study strongly supports symmetric exchange as the principal mechanism leading to ferroelectricity since the small non-collinearity of the magnetic moments within chains along c is observed only for the YMn_2O_5 and HoMn_2O_5 compounds. This does not preclude a potential, but much weaker contribution from Dzyaloshinskii-Moriya interactions.

VI. ACKNOWLEDGEMENTS

We would like to thank B. Ouladdiaf and G. McIntyre from the Institut Laue-Langevin (France) for useful discussions, and the valuable help during the D10 experiment and the crystal alignment with the *OrientExpress* instrument. We acknowledge partial support from the European Commission ("Construction of New Infrastructures", ISIS Target Station II, contract no. 011723).

VII. NOTE ADDED IN PROOF

During the final elaboration of this paper, we became aware of a recent manuscript by H. Kimura *et al.*, which is now in print [31]. Kimura *et al.* investigated the crystal and magnetic structures of YMn_2O_5 , HoMn_2O_5 and ErMn_2O_5 by single crystal neutron diffraction. Although the data analysis methodology is different from ours (they employ a large supercell rather than Fourier components), the agreement with our results on the compounds common to the two studies is excellent. Our work includes the refinement of the BiMn_2O_5 , which, we believe, is crucial in clarifying the correlations between the different spin component and the electrical polarisation.

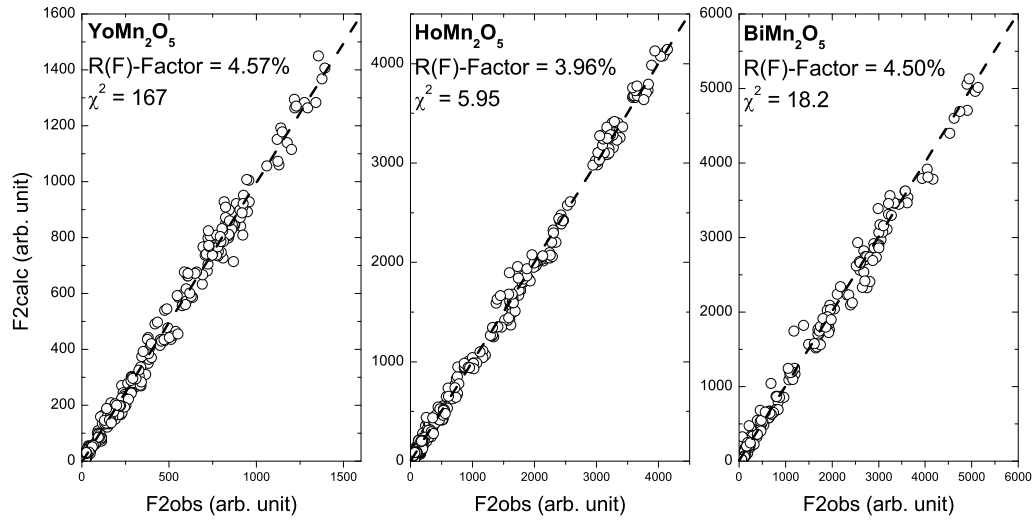


FIG. 1: Results of the refinement for the commensurate magnetic structures for three compounds- YMn_2O_5 , $HoMn_2O_5$ and $BiMn_2O_5$. The experimental structure factors (times a scale factor) are plotted against the calculated ones. The agreement factors- magnetic R(F) factors and χ^2 - are shown. See text for details of the magnetic models.

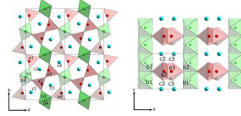


FIG. 2: (Color Online) Crystal structure of RMn_2O_5 projected in the ab -plane (left panel) and ac -plane (right panel). Green, red and blue spheres correspond to Mn^{4+} , Mn^{3+} and R^{3+} ions, respectively. Mn-O polyhedra are shown with the same color scheme. The thin black line represent the crystallographic unit-cell. Correspondence between the labels and atomic positions are described in Table III.

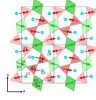


FIG. 3: (Color Online) Magnetic structure of YMn_2O_5 projected in the ab plane. The structure is shown in two unit-cells, marked by thin black lines, along the a - and b -axis. The green and red arrows represent magnetic moments on Mn^{4+} and Mn^{3+} sites respectively. Corresponding Mn-O polyhedra are shown with the same colors. Blue spheres represent Y ions. The different sites are labeled according to Table II.

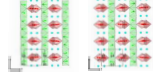


FIG. 4: (Color Online) Magnetic structure of YMn_2O_5 projected in the ac -plane shown within four unit-cells along c and two unit-cells along a . The projection is shown separately for magnetic sites belonging to the first AFM chain (left) and the second chain (right) (See text for details). The green and red arrows represent magnetic moments on Mn^{4+} and Mn^{3+} sites respectively. Corresponding Mn-O polyhedra are shown with the same colors. Blue spheres represent Y ions. The different sites are labeled according to Table II.

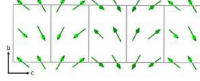


FIG. 5: Magnetic structure of YMn_2O_5 projected in the bc -plane and showing only the Mn^{4+} moments. The figure shows the small helicoidal modulation generated by the out-of-phase c -component. To highlight this weak modulation, the moment have been scaled by a factor five with respect to what represented in the other Figures.

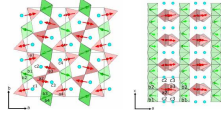


FIG. 6: (Color Online) Magnetic structure of YMn_2O_5 projected in the ab -plane (left panel) and the ac -plane (right panel) for the second domain, obtained by applying inversion symmetry on the magnetic structure of the first domain (Fig. 3, 4)

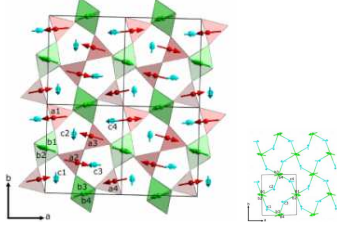


FIG. 7: (Color Online) Magnetic structure of $HoMn_2O_5$ projected in the ab plane. The structure is shown in two unit-cells, marked by thin black lines, along the a - and b -axis. The green, red and blue arrows (left panel) represent magnetic moments on Mn^{4+} , Mn^{3+} and Ho^{3+} sites respectively. Corresponding Mn-O polyhedra are shown with the same colors. For clarity, in the right panel only Mn^{4+} and Ho^{3+} (belonging to an ordered Ho layer) magnetic moments are shown respectively in green and blue color. Lines connecting Mn^{4+} and Ho^{3+} represent interactions (See text for details). The different sites are labeled according to Table III.

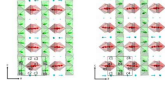


FIG. 8: (Color Online) Magnetic structure of $HoMn_2O_5$ projected in the ac plane shown within four unit-cells along c and two unit-cells along a . The projection is shown separately for magnetic sites belonging to the first AFM chain (left) and the second chain (right) (See text for details). The green, red and blue arrows represent magnetic moments on Mn^{4+} , Mn^{3+} and Ho^{3+} sites respectively. Corresponding Mn-O polyhedra are shown with the same colors. The different sites are labeled according to Table III.

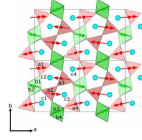


FIG. 9: (Color Online) Magnetic structure of $BiMn_2O_5$ projected in the ab plane. The structure is shown in two unit-cells, marked by thin black lines, along the a - and b -axis. The green and red arrows represent magnetic moments on Mn^{4+} and Mn^{3+} sites respectively. Corresponding Mn-O polyhedra are shown with the same colors. Blue spheres represent Bi ions. The different sites are labeled according to Table IV.

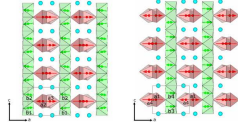


FIG. 10: (Color Online) Magnetic structure of $BiMn_2O_5$ projected in the ac plane shown within four unit-cells along c and two unit-cells along a . The projection is shown separately for magnetic sites belonging to the first AFM chain (left) and the second chain (right) (See text for details). The green and red arrows represent magnetic moments on Mn^{4+} and Mn^{3+} sites respectively. Corresponding Mn-O polyhedra are shown with the same colors. Blue sphere represent Bi ions. The different sites are labeled according to Table IV

Symmetry operation	Domain generated
$\{1 000\}$	D1
$\{\bar{1} 000\} *$	D2
$\{m_{xy}0 000\} *$	D1
$\{2_z 000\}$	D2
$\{m_{0yz} 0\frac{1}{2}0\}$	D1
$\{m_{x0z} \frac{1}{2}00\}$	D2
$\{2_{x00} \frac{1}{2}00\} *$	D2
$\{2_{0y0} 0\frac{1}{2}0\} *$	D1

TABLE I: Action of the symmetry operations of the paramagnetic group on the magnetic structure of domain 1. Domain one and two are abbreviated by D1 and D2. Symmetry operations are shown in the Seitz notation. The * symbol indicates combination of the symmetry operation with complex conjugation operation.

Label	Atom	Position	M_x	M_y	I_z	Ph
b1	Mn^{4+}	(0 0.5 0.25513)	2.01(5)	-0.47(8)	0.36(11)	0.095(2)
b2	Mn^{4+}	(0 0.5 0.74487)	2.13(5)	-0.53(9)	0.44(11)	0.156(2)
b3	Mn^{4+}	(0.5 0 0.25513)	-2.07(5)	-0.53(8)	0.4(1)	0.095(2)
b4	Mn^{4+}	(0.5 0 0.74487)	-1.99(5)	-0.51(8)	0.45(11)	0.156(2)
a1	Mn^{3+}	(0.08805 0.85079 0.5)	3.16(6)	0.59(9)	-0.46(12)	0.125
a2	Mn^{3+}	(0.41195 0.35079 0.5)	-3.18(6)	0.55(9)	-0.50(12)	0.125
a3	Mn^{3+}	(0.58805 0.64921 0.5)	3.01(5)	-0.67(9)	0.56(13)	0.125
a4	Mn^{3+}	(0.91195 0.14921 0.5)	2.99(5)	0.65(9)	-0.60(13)	0.125

TABLE II: Magnetic Fourier coefficients obtained from least-square refinements of the single crystal diffraction data for $Y Mn_2 O_5$ at $T = 25 K$ (See text for details). The Fourier coefficients for each site in the primitive unit-cell are given along crystallographic direction (x,y,z) and labeled M and I when real and imaginary, respectively. The phase for each site (Ph.) is given in units of 2π . Error bars are given for all parameters within parenthesis.

Label	Atom	Position	M_x	M_y	I_z	Ph
b1	Mn^{4+}	(0 0.5 0.2558)	-2.25(4)	0.58(5)	-0.38(8)	0.088(2)
b2	Mn^{4+}	(0 0.5 0.7442)	-2.32(4)	0.59(5)	-0.39(8)	0.161(2)
b3	Mn^{4+}	(0.5 0 0.2558)	2.26(4)	0.59(5)	-0.51(8)	0.088(2)
b4	Mn^{4+}	(0.5 0 0.7442)	2.19(4)	0.55(5)	-0.49(8)	0.161(2)
a1	Mn^{3+}	(0.0885 0.849 0.5)	-3.53(4)	-0.43(5)	0.58(9)	0.125
a2	Mn^{3+}	(0.4115 0.349 0.5)	3.49(4)	-0.73(5)	0.46(9)	0.125
a3	Mn^{3+}	(0.5885 0.651 0.5)	-3.29(4)	0.85(6)	-0.60(8)	0.125
a4	Mn^{3+}	(0.9115 0.151 0.5)	-3.27(4)	-0.72(6)	0.65(8)	0.125
c1	Ho^{3+}	(0.1392 0.1713 0)	0.03(3)	-1.09(4)	0.18(7)	-0.001(2)
c2	Ho^{3+}	(0.3608 0.6713 0)	-0.03(3)	-1.14(4)	0.16(6)	-0.001(2)
c3	Ho^{3+}	(0.6392 0.3284 0)	-1.27(4)	-0.04(4)	-0.16(6)	-0.001(2)
c4	Ho^{3+}	(0.8606 0.8287 0)	-1.25(4)	-0.08(4)	0.24(6)	-0.001(2)

TABLE III: Magnetic Fourier coefficients obtained from least-square refinements of the single crystal diffraction data for $HoMn_2O_5$ at $T = 25 K$ (See text for details). The Fourier coefficients for each site in the primitive unit-cell are given along crystallographic direction (x,y,z) and labeled M and I when real and imaginary, respectively. The phase for each site (Ph.) is given in units of 2π . Error bars are given for all parameters within parenthesis.

Label	Atom	Position	M_x	M_y	M_z	Ph
b1	Mn^{4+}	(0 0.5 0.2613)	2.10(3)	-0.33(6)	0.25(6)	0.0
b2	Mn^{4+}	(0 0.5 0.7387)	2.10(3)	-0.33(6)	-0.25(6)	0.0
b3	Mn^{4+}	(0.5 0 0.2613)	2.07(3)	0.56(6)	0.08(6)	0.0
b4	Mn^{4+}	(0.5 0 0.7387)	2.07(3)	0.56(6)	-0.08(6)	0.0
a1	Mn^{3+}	(0.0926 0.8516 0.5)	-2.83(5)	-0.23(10)	0.000	0.0
a2	Mn^{3+}	(0.4074 0.3516 0.5)	-2.83(5)	0.33(10)	0.000	0.0
a3	Mn^{3+}	(0.5926 0.6484 0.5)	2.80(5)	-0.34(9)	0.000	0.0
a4	Mn^{3+}	(0.9074 0.1484 0.5)	-2.74(5)	-0.64(10)	0.000	0.0

TABLE IV: Magnetic Fourier coefficients obtained from least-square refinements of the single crystal diffraction data for $BiMn_2O_5$ at $T = 10$ K (See text for details). The Fourier coefficients for each site (M, real) in the primitive unit-cell are given along crystallographic direction (x,y,z). The phase for each site (Ph.) is given in units of 2π . Error bars are given for all parameters within parenthesis.

-
- [1] T. Kimura, T. Goto, H. Shintani, K. Ishizaka, T. Arima, and Y. Tokura, *Nature* **426**, 55 (2003).
- [2] N. Hur, S. Park, P. A. Sharma, J. S. Ahn, S. Guha, and S.-W. Cheong, *Nature* **429**, 392 (2004).
- [3] S.-W. Cheong and M. Mostovoy, *Nature Mater.* **6**, 13 (2007).
- [4] I. Kagomiya, S. Matsumoto, K. Khon, Y. Fukuda, T. Shoubu, H. Kimura, Y. Noda, and N. Ikeda, *Ferroelectrics* **286**, 889 (2003).
- [5] W. Eerenstein, N. D. Mathur, and J. F. Scott, *Nature* **442**, 759 (2006).
- [6] A. F. Garca-Flores, E. Granado, H. Martinho, C. Rettori, E. I. Golovenchits, V. A. Sanina, S. B. Oseroff, S. Park, and S.-W. Cheong, *J. Appl. Phys.* **101**, 09M106 (2007).
- [7] R. V. Aguilar, A. B. Sushkov, S. Park, S.-W. Cheong, and H. D. Drew, *Phys. Rev. B* **74**, 184404 (2006).
- [8] Y. Noda, H. Kimura, Y. Kamada, T. Osawa, Y. Fukuda, Y. Ishikawa, S. Kobayashi, Y. Wakabayashi, H. Sawa, N. Ikeda, et al., *Phys. B* **385**, 119 (2006).
- [9] T.-C. Han and J. G. Lin, *J. Appl. Phys.* **99**, 08J508 (2006).
- [10] J. G. Lin, T.-C. Han, and C.-H. Chen, *IEEE Trans. Magn.* **41**, 3440 (2005).
- [11] O. Prokhnenko, R. Feyerherm, E. Dudzik, S. Landsgesell, N. Aliouane, L. C. Chapon, and D. N. Argyriou, *Phys. Rev. Lett.* **98**, 057206 (2007).
- [12] J. Koo, C. Song, S. Ji, J. S. Lee, J. Park, T. H. Jang, C. H. Yang, J. H. Park, Y. H. Jeong, K. B. Lee, et al., *Non-resonant and resonant x-ray scattering studies on multiferroic tbmn2o5* (2007), URL <http://www.citebase.org/abstract?id=oai:arXiv.org:0704.0533>.
- [13] D. I. Khomskii, *J. Magn. Magn. Mater* **306**, 1 (2006).
- [14] Y. Yamasaki, H. Sagayama, T. Goto, M. Matsuura, K. Hirota, T. Arima, and Y. Tokura, *Phys. Rev. Lett.* **98**, 147204 (2007).
- [15] G. Lawes, A. B. Harris, T. Kimura, N. Rogado, R. J. Cava, A. Aharony, O. Entin-Wohlman, T. Yildirim, M. Kenzelmann, C. Broholm, et al., *Phys. Rev. Lett.* **95**, 087205 (2005).
- [16] L. C. Chapon, P. G. Radaelli, G. R. Blake, S. Park, and S.-W. Cheong, *Phys. Rev. Lett.* **96**, 097601 (2006).
- [17] I. A. Sergienko, C. Sen, and E. Dagotto, *Phys. Rev. Lett.* **97**, 227204 (2006).

- [18] C. Wilkinson, F. Sinclair, P. Gardner, J. B. Forsyth, and B. M. R. Wanklyn, *J. Phys. C: Solid State Phys.* **14**, 1671 (1981).
- [19] P. P. Gardner, C. Wilkinson, J. B. Forsyth, and B. M. Wanklyn, *J. Phys. C: Solid State Phys.* **21**, 5653 (1988).
- [20] W. R. II, V. Kiryukhin, M. Kenzelmann, S.-H. Lee, R. Erwin, J. Schefer, N. Hur, S. Park, and S.-W. Cheong, *Phys. Rev. B* **72**, 0600407 (2005).
- [21] A. Muñoz, J. A. Alonso, M. T. Casais, M. J. Martínez-Lope, J. L. Martínez, and M. Fernández-Díaz, *Phys. Rev. B* **65**, 144423 (2002).
- [22] J. Rodriguez-Carvajal, *Physica B* **192**, 55 (1993).
- [23] G. R. Blake, L. C. Chapon, P. G. Radaelli, S. Park, N. Hur, S.-W. Cheong, and J. Rodriguez-Carvajal, *Phys. Rev. B* **71**, 214402 (2005).
- [24] P. G. Radaelli and L. C. Chapon, *Phys. Rev. B* **76**, 054428 (2007).
- [25] J. Pannetier, J. Bassas-Alsina, J. Rodriguez-Carvajal, and V. Caignaert, *Nature* **346**, 343 (1990).
- [26] G. Amoretti, R. Caciuffo, Santini, O. Francescangeli, E. Goremychkin, R. Osborn, G. Calestani, M. Sparpaglione, and L. Bonoldi, *Physica C* **221**, 227 (1994).
- [27] L. C. Chapon, G. R. Blake, M. J. Gutmann, S. Park, N. Hur, P. G. Radaelli, and S.-W. Cheong, *Phys. Rev. Lett.* **93**, 177402 (2004).
- [28] A. B. Sushkov, R. V. Aguilar, S. Park, S.-W. heon, and H. D. Drew, *Phys. Rev. Lett.* **98**, 027202 (2007).
- [29] C. R. dela Cruz, F. Yen, B. Lorenz, S. Park, S.-W. Cheong, M. M. Gospodinov, W. Ratcliff, J. W. Lynn, and C. W. Chu, *J. Appl. Phys.* **99**, 08R103 (2006).
- [30] H. Katsura, N. Nagaosa, and A. V. Balatsky, *Phys. Rev. Lett.* **95**, 057205 (2005).
- [31] H. Kimura, S. Kobayashi, Y. Fukuda, T. Osawa, Y. Kamada, Y. Noda, I. Kagomiya, and K. Kohn, *J. Phys. Society Japan* **76**, 074706 (2007).
- [32] Ionic radius for a valence of 3+ and 8-coordinated configuration
- [33] R(F) factor is defined as: $R(F) = 100\{\sum_{\mathbf{h}} |F_{obs,\mathbf{h}} - F_{calc,\mathbf{h}}|\}/\{\sum_{\mathbf{h}} |F_{obs,\mathbf{h}}|\}$, where F_{obs} and F_{calc} are respectively the observed and calculated structure factors for a given reflection \mathbf{h}